nature energy

ARTICLES

https://doi.org/10.1038/s41560-022-00988-w

Check for updates

Ta–TiO_x nanoparticles as radical scavengers to improve the durability of Fe–N–C oxygen reduction catalysts

Hua Xie[1,7], Xiaohong Xie[2,7], Guoxiang Hu[3]✉, Venkateshkumar Prabhakaran[2], Sulay Saha[4], Lorelis Gonzalez-Lopez[1], Abhijit H. Phakatkar[5], Min Hong[1], Meiling Wu[1], Reza Shahbazian-Yassar[5]✉, Vijay Ramani[4], Mohamad I. Al-Sheikhly[1], De-en Jiang[6], Yuyan Shao[2]✉ and Liangbing Hu[1]✉

Highly active and durable platinum group metal-free catalysts for the oxygen reduction reaction, such as Fe–N–C materials, are needed to lower the cost of proton-exchange membrane fuel cells. However, their durability is impaired by the attack of oxidizing radicals such as ·OH and HO_2· that form from incomplete reduction of O_2 via H_2O_2. Here we demonstrate that Ta–TiO_x nanoparticle additives protect Fe–N–C catalysts from such degradation via radical scavenging. The 5 nm Ta–TiO_x nanoparticles were uniformly synthesized on a Ketjenblack substrate using a high-temperature pulse technique, forming the rutile TaO_2 phase. We found that Ta–TiO_x nanoparticles suppressed the H_2O_2 yield by 51% at 0.7 V in an aqueous rotating ring disk electrode test. After an accelerated durability test, a fuel cell prepared with the scavengers showed a current density decay of 3% at 0.9 $V_{iR\text{-}free}$ (internal resistance-compensated voltage); a fuel cell without scavengers showed 33% decay. Thus, addition of Ta–TiO_x provides an active defence strategy to improve the durability of oxygen reduction reaction catalysts.

The design of highly active and durable electrocatalysts for the oxygen reduction reaction (ORR) is of paramount importance for proton-exchange membrane (PEM) fuel cells[1–3]. Platinum group metal-free (PGM-free) catalysts are promising alternatives to current platinum-based materials due to their substantial reduction in overall cost[4–6]. In particular, transition metal and nitrogen co-doped carbon (M–N–C, M = Fe, Co, Mn, Sn and so on) catalysts have been intensively investigated for this purpose because of their high activity[7–9]. However, these state-of-the-art PGM-free catalysts face severe durability issues, particularly in acidic environments in which performance rapidly decays within the first 100 hours of fuel cell operation[10], limiting industrial application[11–13]. There have been limited studies about their degradation mechanisms and recently, scientists have started to pay more attention. Studies show the deteriorating performance of PGM-free catalysts may stem from demetallation, protonation of the N-group and electrochemical carbon corrosion[13–16]. However, attack from ·OH and HO_2· radicals is considered one of the most critical sources of degradation[17].

Radicals such as ·OH and HO_2· can directly damage the active sites in PGM-free catalysts[12,13,18,19] through two pathways: one is the oxidation of carbon to CO_2[17], which can further lead to the demetallation of metal active sites; the other is the formation of oxygen functional groups[14,20], which severely decreases the turnover frequency of catalysts. Additionally, the damaged M–N moieties further lead to a drastic increase of the H_2O_2 yield in acidic media, forming a positive feedback loop that deteriorates the catalytic performance. Although state-of-the-art PGM-free catalysts present good electrocatalytic selectivity and relatively low H_2O_2 yield (generally under 5%), the net generation of radicals due to accumulated intermediate H_2O_2 can still degrade the catalysts and impair their activity[21]. H_2O_2 is usually not considered as the most reactive oxygen species. The ·OH radicals are the most reactive oxygen species. Under some circumstances, such as high temperatures, acid environment and Fenton reaction's conditions, H_2O_2 decomposes into ·OH. Thus, neutralizing the influence of H_2O_2 in an acidic environment is critical to mitigate the degradation of PGM-free catalysts.

Previous strategies to solve this issue have focused on enhancing the catalyst's structural stability. For example, increasing the carbon substrate graphitization has been shown to improve the robustness of PGM-free catalysts and their tolerance to H_2O_2[22,23]. However, it is challenging to retain sufficient activity with this approach as the graphitization treatment often leads to the loss of active sites (that is, M–N moieties)[24–28]. Eliminating the formation of metal particles in the catalysts by reducing the metal precursor loading during synthesis is another strategy, as the metal particles dissolve in the acidic environment and generate metal ions (for example, ferrous ions), which can further catalyse the formation of radicals via Fenton reactions[29,30]. However, this strategy only partially slows the degradation of M–N moieties by H_2O_2. Clearly, approaches that can proactively and directly eliminate H_2O_2 are desired to improve the longevity of PGM-free catalysts in the catalytic oxygen reduction process.

[1]Department of Materials Science and Engineering, University of Maryland, College Park, MD, USA. [2]Pacific Northwest National Laboratory, Richland, WA, USA. [3]Department of Chemistry and Biochemistry, Queens College of the City University of New York, Queens, NY, USA. [4]Center for Solar Energy and Energy Storage and Department of Energy, Environmental and Chemical Engineering, Washington University in St. Louis, St. Louis, MO, USA. [5]Department of Mechanical and Industrial Engineering, University of Illinois at Chicago, Chicago, IL, USA. [6]Department of Chemistry, University of California, Riverside, CA, USA. [7]These authors contributed equally: Hua Xie, Xiaohong Xie. ✉e-mail: guoxiang.hu@qc.cuny.edu; rsyassar@uic.edu; yuyan.shao@pnnl.gov; binghu@umd.edu

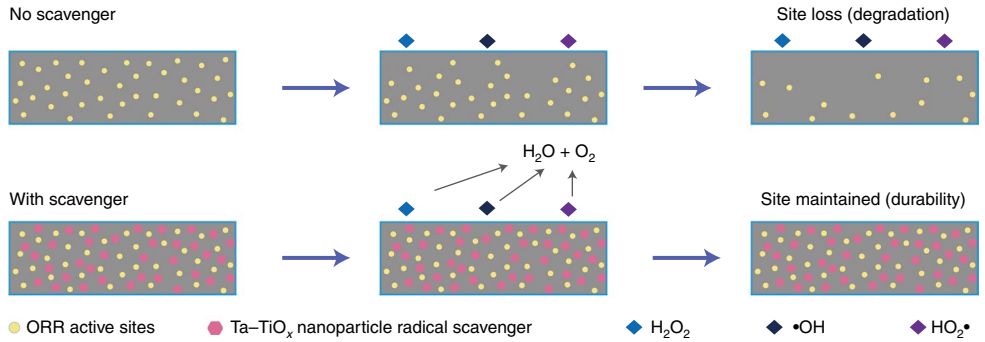

Fig. 1 | Schematic comparing the PGM-free catalyst durability in the ORR process without and with the Ta-TiO_x/Ketjenblack scavengers. Without the scavengers, the ORR performance decays rapidly due to the loss of the catalytic active sites. The introduction of the Ta-TiO_x scavengers can proactively decompose the ·OH, HO_2· and H_2O_2 generated in the incomplete oxygen reduction pathway. The grey background is the catalyst coating in fuel cells. ORR active sites and Ta-TiO_x nanoparticles are uniformly distributed in the coating.

Herein we report a approach for addressing this catalyst degradation issue by introducing Ta–TiO_x nanoparticle additives to the PGM-free catalyst to serve as scavengers for radicals and H_2O_2, which improves the catalytic durability. This nanoparticle radical scavenging concept provides an approach for improving ORR catalyst durability from passive shielding to an active defence in which H_2O_2 and radicals are proactively removed. The strategy also could be applied to other systems that involve detrimental oxygen radicals such as organic synthesis and cell recoveries to control the influence of H_2O_2 and its radicals.

The Ta-TiO_x radical scavengers

Figure 1 illustrates a comparison of the PGM-free catalyst behaviour towards ·OH, HO_2· and H_2O_2 without and with the Ta–TiO_x scavengers in the oxygen reduction process. After the PGM-free catalyst produces H_2O_2 due to incomplete reduction of oxygen, the scavenger nanoparticles decompose the molecules into H_2O and O_2 via a disproportionation reaction[31] (Supplementary Fig. 1).

We employed a high-temperature pulse approach to synthesize the supported Ta–TiO_x nanoparticles[32]. Titanium(IV) isopropoxide and tantalum(V) ethoxide mixed with the carbon substrate were sonicated in ethanol and deionized water to form a slurry mixture (Methods). After freeze drying, the mixture was subjected to a fast high-temperature treatment (~1,500 K) by Joule heating in an argon environment for 100 ms and then quenching the reaction by cooling at an initial rate of 10^5 K s^{-1} to achieve the uniformly dispersed oxide nanoparticles on the carbon substrate (schematically shown in Fig. 2a). Figure 2b shows a scanning electron micrograph (SEM) of the supported Ta–TiO_x nanoparticles on a Ketjenblack substrate (KB; the Ta to Ti ratio is 6:4). The carbon substrate provides ample pores and surfaces to anchor the Ta–TiO_x nanoparticles and promotes their dispersion. Thermogravimetric analysis results show the nanoparticles are around 66 wt% to the total weight of Ta–TiO_x/KB (Supplementary Fig. 2). Note that this approach can be applied to other substrates as well, such as carbon nanofiber membranes or carbon powders pyrolysed from metal-organic frameworks (Supplementary Fig. 3). Figure 2c and Supplementary Fig. 4 show the transmission electron micrographs (TEM) of the Ta–TiO_x nanoparticles, which feature a size distribution of 5.2 ± 1.2 nm (Fig. 2d). High-angle annular dark-field scanning transmission electron microscopy (HAADF-STEM) of the nanoparticles revealed lattice fringes of 0.38 nm and 0.37 nm, corresponding to the (010) and (100) planes of the solid solution structure of tantalum titanium oxide (Fig. 2e). Energy-dispersive X-ray spectroscopy further confirmed the uniform alloying of the Ta and Ti elements in the nanoparticles (Fig. 2f).

We also measured the N_2 adsorption-desorption isotherms of the KB-supported Ta–TiO_x nanoparticles at 77 K to evaluate the specific surface area of the scavengers (Fig. 2g). The material demonstrated a surface area of 312.7 $m^2 g^{-1}$ as determined by the Brunauer–Emmett–Teller method, which is consistent with the high porosity shown in the SEM and TEM images. Such porosity and uniform dispersion should help enhance the exposure of nanoparticles to H_2O_2 and reduce the net accumulation of ·OH and HO_2· radicals through either efficient scavenging of radicals or chemical decomposition of H_2O_2 to water and oxygen. Moreover, anchoring the oxide nanoparticles on the carbon substrate may help prevent their detachment and deterioration over the course of the ORR.

We synthesized nanoparticles of different Ta to Ti atomic ratios of 2:8, 4:6, 6:4 and 8:2 by tuning the precursor loading (Supplementary Fig. 5). The powder X-ray diffraction (XRD) patterns of the resulting Ta–TiO_x nanoparticles demonstrate the phase evolution of the different compositions (Fig. 2h). As we changed the Ta to Ti ratio from 2:8 to 8:2, the dominant crystal phase gradually evolved from a solid solution of TiO_2 (anatase structure) to Ta_2O_5. However, the Ta–TiO_x nanoparticles with 6:4 Ta to Ti ratio results in the appearance of a rutile TaO_2 structure (marked with asterisks and Supplementary Fig. 6). This rutile solid solution can be generated in an oxygen-deficient environment under fast temperature change[33], made feasible here by the rapid heating and quenching at a rate of 10^5 K s^{-1} during synthesis. Rutile TaO_2 is metastable and its surface can strongly adsorb oxygen or hydroxy groups, forming the stable cation-deficient compound $Ta_{0.8}O_2$, while the structure remains rutile with only minor changes of the lattice constants[33]. The X-ray photoelectron spectroscopy analysis confirmed no discernable valence change of the Ta ions as the atomic ratios were varied (Supplementary Fig. 7). The distinct phase structures of these Ta–TiO_x nanoparticles can present substantial differences in radical scavenging capabilities.

Radical scavenging performance

To quantitatively determine the radical scavenging efficacy of the as-prepared Ta–TiO_x/KB (Ta to Ti ratio of 6:4), we employed an ex situ custom-built fluorescence spectrometer to monitor for changes in radical concentration. An Fe–N–C catalyst was synthesized via pyrolysis of an Fe-containing zeolitic imidazolate framework (ZIF-8) to serve as a representative PGM-free catalyst. This PGM-free catalyst mainly contains atomically dispersed active centres with a small amount of Fe-carbide side phase according to our previous Mössbauer measurements[11]. We used 6-carboxy fluorescein (6CFL) dye, which is known to be sensitive to radicals and degrade under their attack, as a fluorescent molecular

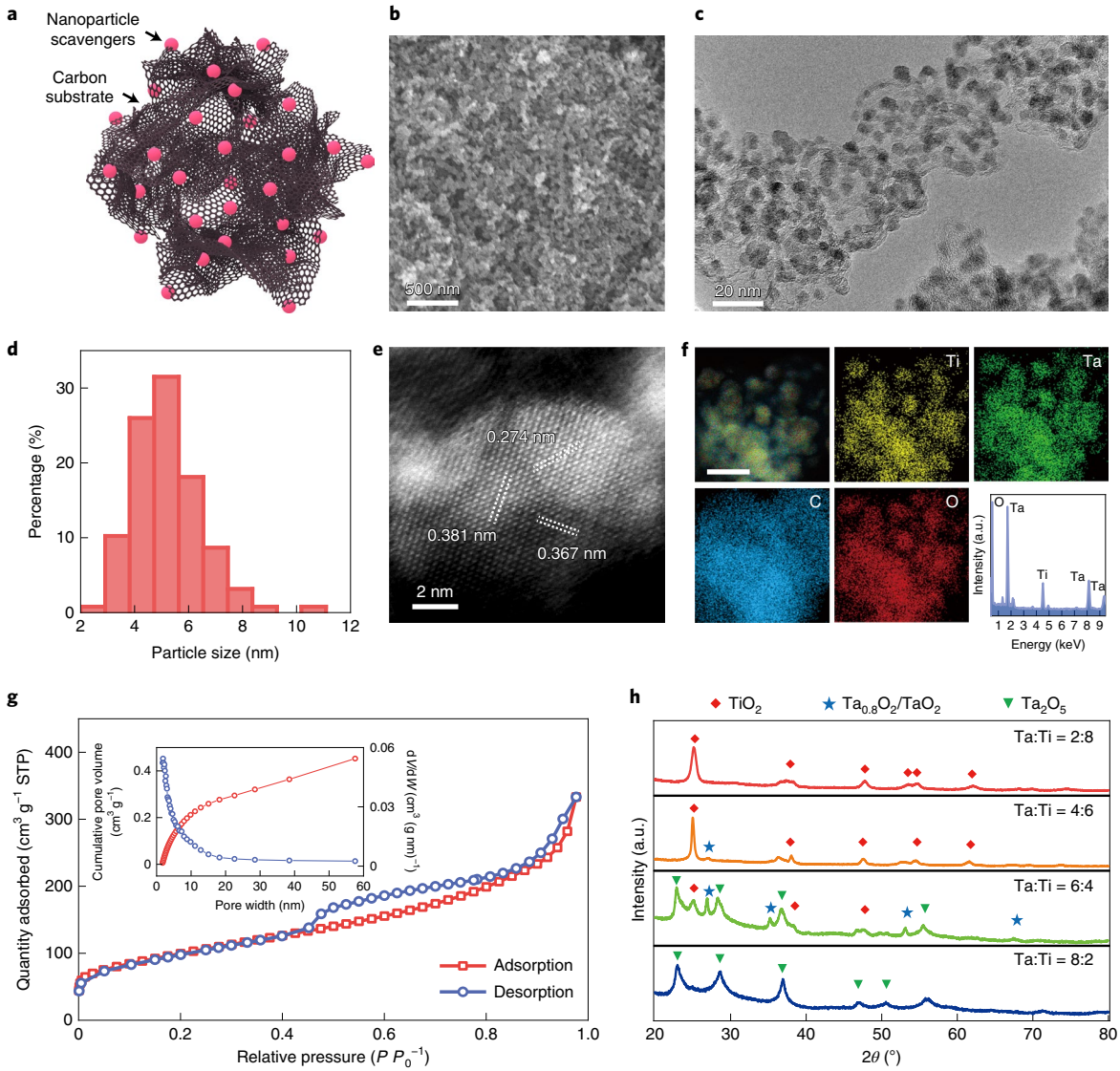

Fig. 2 | Morphology of the Ta–TiO$_x$ radical scavengers. a, Schematic demonstrating the well-dispersed Ta–TiO$_x$ nanoparticles on the carbon substrate as scavengers. **b**, SEM image of the Ta–TiO$_x$ nanoparticles on KB, demonstrating the material's high porosity. **c**, TEM image of the Ta–TiO$_x$ nanoparticles, which feature uniform dispersion on the substrate. **d**, The size distribution of the Ta–TiO$_x$ nanoparticles. **e**, HAADF-STEM image of the Ta–TiO$_x$ nanoparticle in a [001] zone axis. The white dashed lines indicate the lattice distances. **f**, Energy-dispersive X-ray spectroscopy elemental mapping of the Ta–TiO$_x$ nanoparticles showing the successful alloying of the two oxides. Scale bar, 20 nm. The graph in the bottom right corner shows the energy-dispersive X-ray spectroscopy profile of the Ta–TiO$_x$ nanoparticles. **g**, N_2 adsorption-desorption isotherms of the KB-supported Ta–TiO$_x$ nanoparticles at 77 K. Inset: pore size distribution. STP, standard temperature and pressure. **h**, Powder X-ray diffraction patterns of the nanoparticles synthesized with Ta to Ti ratios of 2:8, 4:6, 6:4 and 8:2. A rutile tantalum oxide phase was detected when the ratio was 6:4.

probe[34,35]. Fenton's reagent was used as the radical source solution. We compared the 6CFL fluorescence decay after adding only Fenton's reagent, Fenton's reagent/Fe–N–C and Fenton's reagent/Ta–TiO$_x$ scavengers, respectively. The raw fluorescence spectra and plots of the fluorescence intensity of these three scenarios at 544 nm are shown in Supplementary Figs. 8 and 9, respectively. The Stern–Volmer plot in Fig. 3a indicates a substantially higher fluorescence decay of 6CFL for the scenario with only Fenton's reagent or Fenton's reagent/Fe–N–C compared with the measurement with Fenton's reagent/Ta–TiO$_x$. We attribute this decreased fluorescence decay of the Fenton's reagent/Ta–TiO$_x$ sample to the higher radical scavenging ability of the Ta–TiO$_x$ nanoparticles, which decreases the oxidation of the 6CFL molecular probe. These results clearly demonstrate that Ta–TiO$_x$/KB presents high efficiency at scavenging generated radicals compared with Fe–N–C.

Electron paramagnetic resonance (EPR) spin trapping measurements were also conducted to experimentally demonstrate the scavenging capability of the Ta–TiO$_x$ for ·OH radicals with 5,5-dimethyl-1-pyrroline-*N*-oxide (DMPO) as the spin trap. Fenton's reagent was used to generate the ·OH radicals. Figure 3b shows the EPR spectra of OH–DMPO· in the absence and presence of Ta–TiO$_x$/KB. The EPR peak intensity with Ta–TiO$_x$/KB is notably decreased in comparison with that without Ta–TiO$_x$/KB. In addition, despite the decrease in [OH–DMPO·], there is no change in the hyperfine structure of the EPR spectrum, which is identical to previously published OH–DMPO· results[36]. This strongly suggests that the ·OH radicals are scavenged by Ta–TiO$_x$. Additionally, we measured the concentration in spins per gram of the OH–DMPO· adduct in the Fenton's reagent with and without the addition of Ta–TiO$_x$/KB. Figure 3c shows the decay kinetics of the OH–DMPO· as a function of time with and

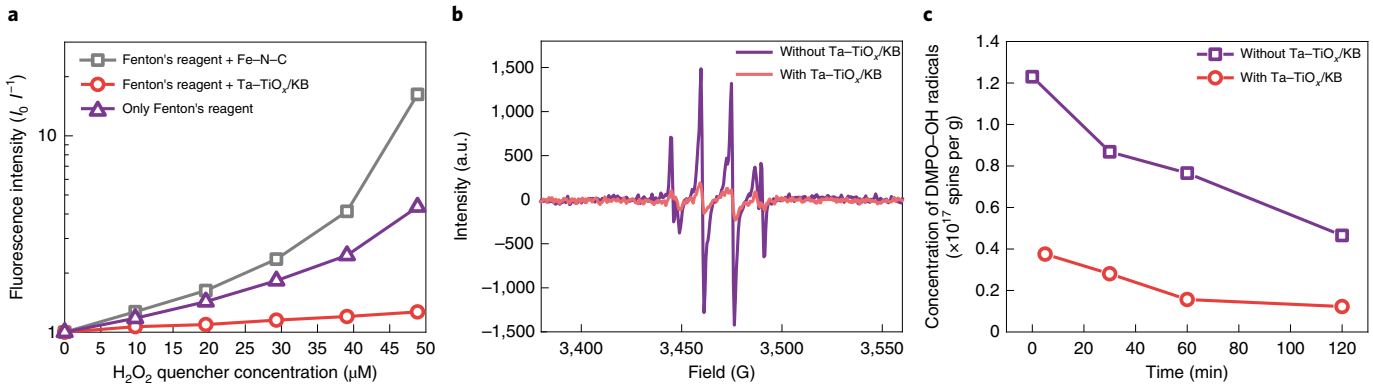

Fig. 3 | The radical scavenging performance of Ta-TiO$_x$/KB. a, Stern-Volmer plot obtained using 6CFL dye in the radical solution containing Fenton's reagent and Fe-N-C or Ta-TiO$_x$ scavengers as a function of the H_2O_2/radical quencher concentration. **b**, Electron paramagnetic resonance spectra of the OH-DMPO· radical with and without the addition of Ta-TiO$_x$/KB to the solution. **c**, Decay in the concentration of the OH-DMPO· radical, with and without the addition of Ta-TiO$_x$/KB, as a function of time.

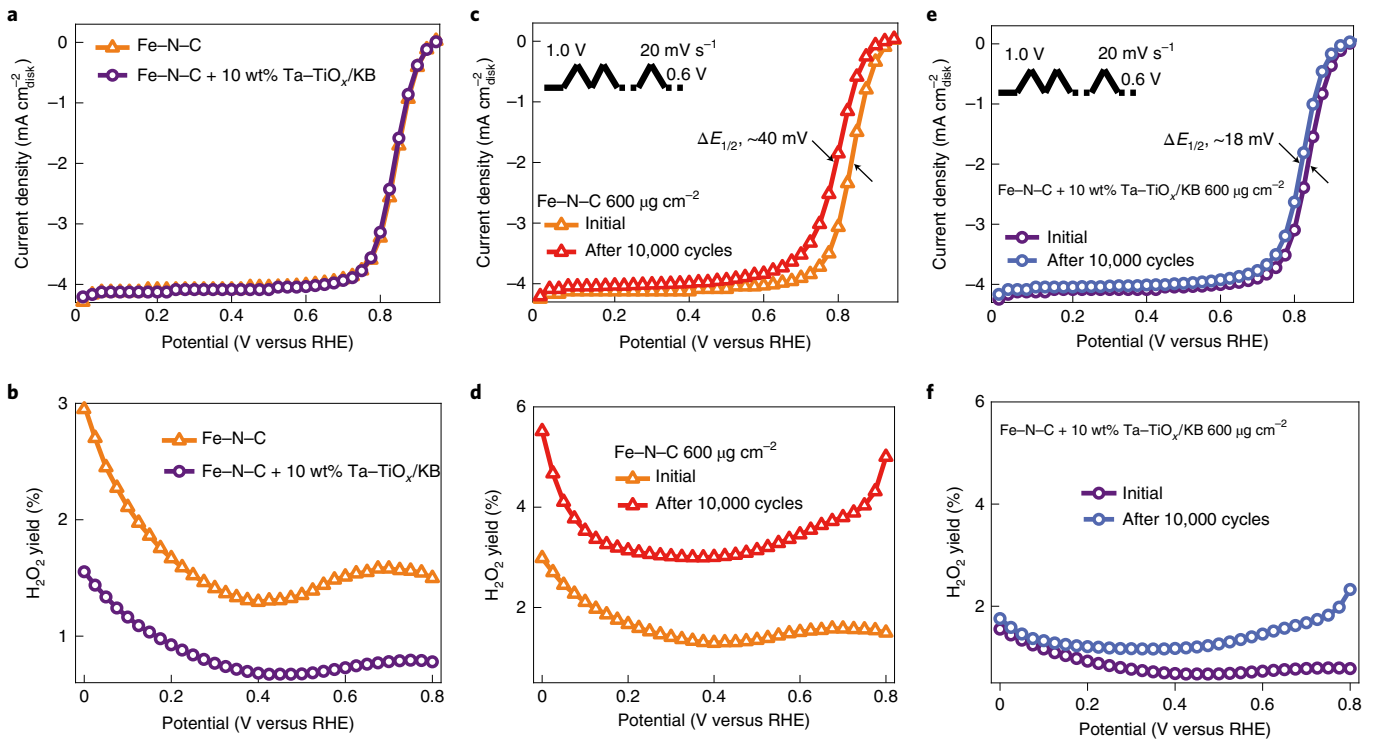

Fig. 4 | The Fe-N-C catalyst protection and H_2O_2 suppression performance of the Ta-TiO$_x$/KB scavengers. a,**b**, The ORR performance (**a**) and H_2O_2 yield (**b**) of the Fe-N-C catalyst with and without the Ta-TiO$_x$/KB scavengers (10 wt%, Ta to Ti ratio = 6:4). **c**, The RRDE durability test of the Fe-N-C catalyst without the scavengers, showing the ORR performance at the initial cycle and after 10,000 potential cycles. **d**, The H_2O_2 yield of the Fe-N-C catalyst without the scavengers at 1 and 10,000 potential cycles. **e**, The durability test of the Fe-N-C catalyst with the scavengers (10 wt%, Ta to Ti ratio = 6:4). **f**, The H_2O_2 yield of the Fe-N-C catalyst with the scavengers at 1 and 10,000 potential cycles.

without Ta–TiO$_x$/KB. We note the low concentration of [OH–DMPO·] in the presence of the Ta–TiO$_x$ radical scavengers in which the process well fits a second-order decay (Supplementary Fig. 10).

We characterized the electrocatalytic behaviour of the Ta–TiO$_x$ scavengers in the presence of the Fe–N–C catalyst to evaluate their H_2O_2 and radical removing ability in the oxygen reduction process. The Fe–N–C catalyst and Ta–TiO$_x$/KB were mixed to form an ink (Supplementary Fig. 11) and deposited on a rotating ring disk electrode (RRDE). A potential of 1.3 V (versus a reversible hydrogen electrode, RHE) was then applied on the ring electrode in O_2-saturated 0.5 M H_2SO_4 electrolyte to quantitatively capture the relative H_2O_2 yield. Figure 4a presents the ORR activity of the Fe–N–C catalyst with and without 10 wt% of the scavengers, synthesized at a Ta to Ti ratio of 6:4 (the other ratios are shown in Supplementary Fig. 12). The RRDE test revealed a half-wave potential of 0.84 V (versus RHE) for the Fe–N–C catalyst without the scavengers, showing a well-defined mass transport-limiting current density. The introduction of the 10 wt% Ta–TiO$_x$/KB at a Ta to Ti ratio of 6:4 initially presents no discernable influence on the catalytic activity, which indicates the material's good compatibility with the Fe–N–C catalyst.

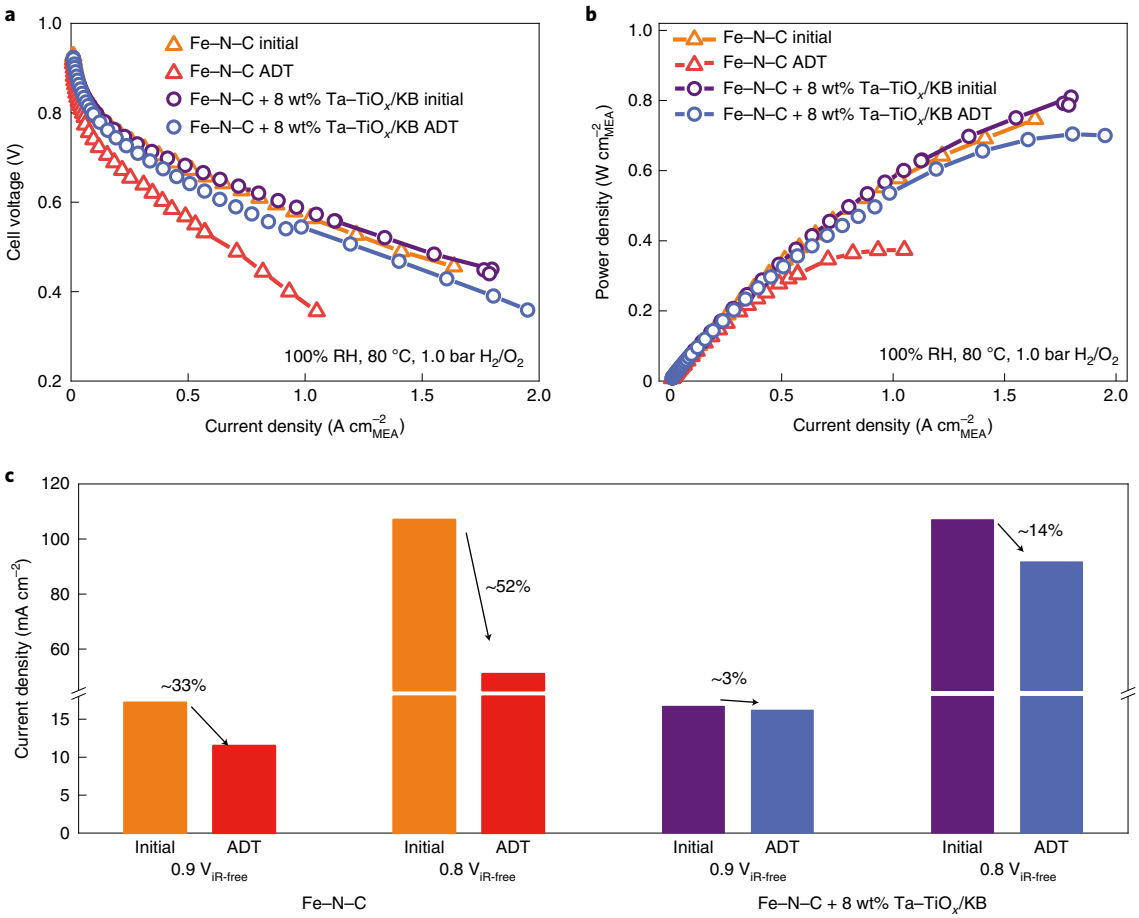

Fig. 5 | PEM fuel cell performances of the PGM-free cathode with and without Ta–TiO$_x$/KB. a,**b**, Voltage (**a**) and power density polarization (**b**) for cells before and after the ADT. Cathode, Fe-N-C catalyst loading of 6.0 mg cm^{-2} (with or without scavengers); anode, Pt/C (Tananka K.K., 46.5% Pt) catalyst loading of 0.2 mg$_{Pt}$ cm^{-2}; MEA, membrane electrode assembly; RH, relative humidity. **c**, Current density decay comparison for cells with and without Ta-TiO$_x$/KB after the ADT. The Ta-TiO$_x$ scavengers substantially elevated the durability of the fuel cells.The *y*-axis break is used to enhance readability for small current density values.

Figure 4b shows the H_2O_2 yield with and without 10 wt% Ta–TiO$_x$/KB at a Ta to Ti ratio of 6:4. The initial H_2O_2 yield for the Fe–N–C catalyst without Ta–TiO$_x$/KB was ~1.6% at an electrode potential of 0.7 V (versus RHE). The relatively low H_2O_2 yield is attributed to the high catalytic efficiency of the Fe–N$_4$ moieties in the catalyst[14], which feature a high average electron transfer number per O_2 molecule (n_e). The H_2O_2 yield presents a gradual increase with the decrease of Fe–N–C catalyst loading from 0.600 mg cm^{-2} to 0.075 mg cm^{-2} (Supplementary Fig. 13). After the introduction of the Ta–TiO$_x$/KB, the H_2O_2 yielded from the catalysts displayed a pronounced decrease that is strongly dictated by the Ta to Ti composition ratio (Fig. 4b and Supplementary Figs. 12 and 13). The Ta–TiO$_x$ scavengers synthesized with a Ta to Ti ratio of 6:4 provide the lowest H_2O_2 yield (around 0.88% at 0.7 V), indicating the highest H_2O_2 removal capability, which is probably attributed to the newly formed $Ta_{0.8}O_2$/TaO_2 solid solution, whereas other compositions present different H_2O_2-removal capabilities with a H_2O_2 yield of 1.3–1.7%. Note that this high scavenging capability corresponds with the rutile tantalum oxide that was formed at the 6:4 ratio as shown in the XRD results. We also varied the Ta–TiO$_x$/KB content from 5 wt% to 20 wt% of the Fe–N–C catalyst to evaluate the influence of scavenger loading on the scavenging ability (Supplementary Fig. 14). At 10 wt% loading, the material demonstrated optimal H_2O_2-removal efficiency.

To evaluate the effect of the Ta–TiO$_x$ scavengers (10 wt%, Ta to Ti ratio of 6:4) on the durability of the catalyst, we subjected Fe–N–C with and without the Ta–TiO$_x$/KB to a continuous voltammetry cycling process for 10,000 cycles between 0.6 V and 1.0 V with a scan rate of 20 mV s^{-1} in an O_2-saturated 0.5 M H_2SO_4 solution. The ORR performance of Fe–N–C without the Ta–TiO$_x$/KB showed the catalyst activity remarkably decayed after cycling with the half-wave potential shifting by 40 mV to a more negative potential value compared with that of the pristine Fe–N–C catalysts (Fig. 4c). Additionally, there was a 3.8% H_2O_2 yield at 0.7 V after cycling the Fe–N–C catalyst without the Ta–TiO$_x$/KB, corresponding to a 2.4-fold increase compared with the initial H_2O_2 yield value (Fig. 4d). We attribute the abnormally high H_2O_2 yield after cycling to the degradation of the Fe–N$_4$ active sites[14] in which the oxidation of carbon to oxygen surface groups can induce H_2O_2 formation in subsequent cycles. In comparison, the Fe–N–C catalyst with the Ta–TiO$_x$ scavengers featured good durability over the 10,000 cycles with a much smaller activity loss of around 18 mV in the half-wave potential shift (Fig. 4e). The H_2O_2 yield also remained around 1.67% at 0.7 V (Fig. 4f), much lower than the value for the Fe–N–C catalyst without Ta–TiO$_x$. These cycling tests clearly demonstrate the ability of the Ta–TiO$_x$ scavengers to remove the generated H_2O_2 and radicals in a rapid and continuous manner.

Fuel cell performance

To further confirm the performance of the scavengers, we conducted an accelerated durability test (ADT) on the PEM fuel cell.

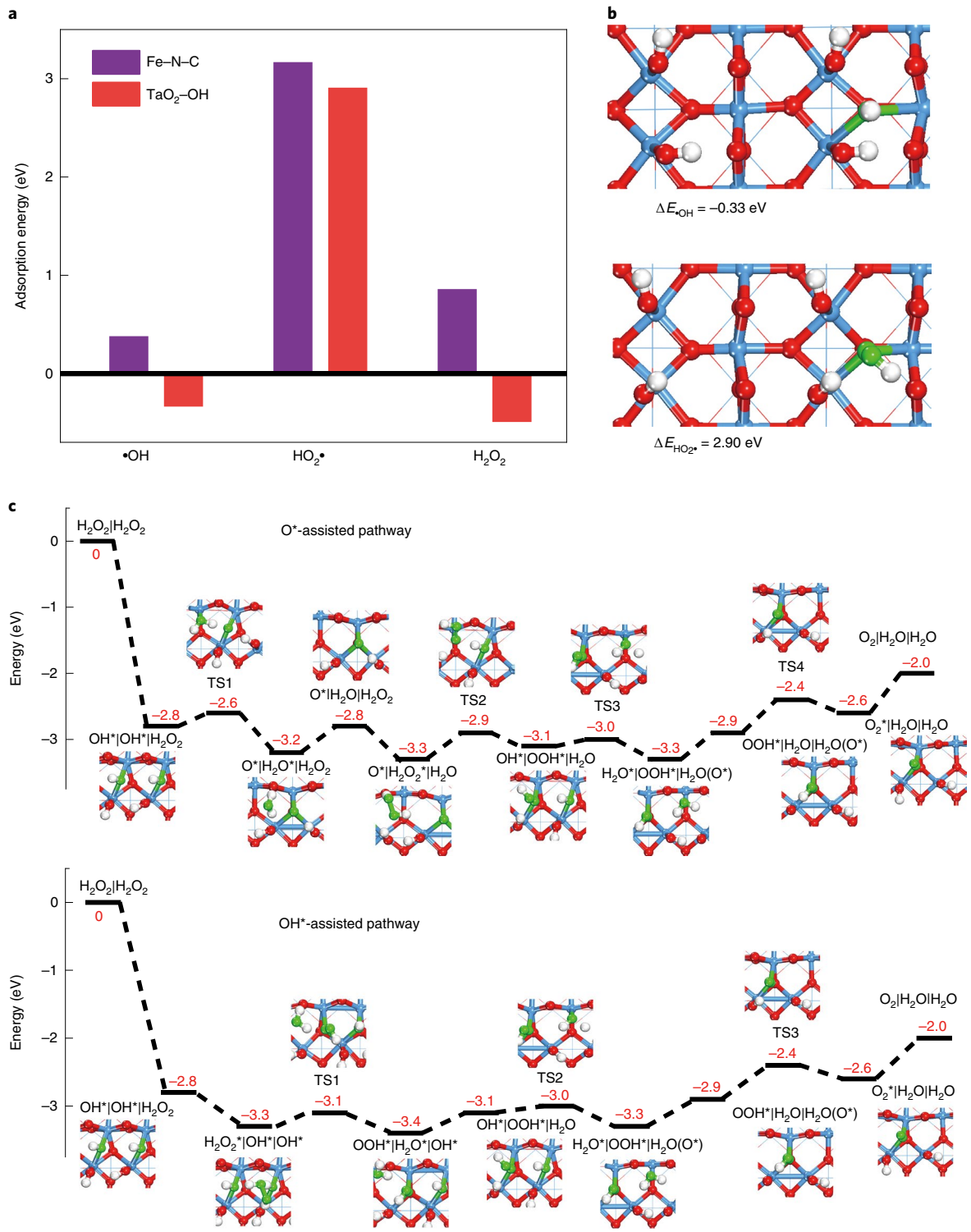

Fig. 6 | DFT calculations to understand the radical scavenging performance of the Ta-TiO_x/KB. a, Adsorption energies of H_2O_2 and related radicals on the surfaces of Fe-N-C and TaO_2-OH. **b**, The adsorption structures and energies (ΔE) of ·OH and HO_2· on TaO_2-OH(110). The cyan and red balls represent Ta and O atoms in TaO_2-OH; the green and white balls represent O and H atoms in the radicals. **c**, OH*- and O*-assisted pathways for the removal of H_2O_2 and related radicals. The OH*- and O*-assisted pathways disperse at the OH* | OH* | H_2O_2 step and converge at the OH* | OOH* | H_2O step. *, denotes adsorption on the surface; |, denotes infinite separation of two adsorbates from each other; TS, transition state. All the represented structures are shown. The atomic colour scheme is the same as in **b**.

Figure 5a,b shows the cell voltage and power density polarization plots of the cells operated with and without the scavengers at different current densities. After the durability test, the fuel cell with the Ta–TiO_x/KB scavengers maintained a current density of 0.63 A cm^{-2} at 0.6 V and achieved a peak power of 700 mW cm^{-2}, which outperforms the cell fabricated without scavengers (0.39 A cm^{-2} at 0.6 V

and 370 mW cm^{-2}). Figure 5c compares the current density of the cells with and without the Ta–TiO_x/KB scavengers at internal resistance-compensated voltages ($V_{iR\text{-}free}$) of 0.8 $V_{iR\text{-}free}$ and 0.9 $V_{iR\text{-}free}$. The cell without the Ta–TiO_x scavengers features a notable current density decay after the durability test of 33% at 0.9 $V_{iR\text{-}free}$ and 52% at 0.8 $V_{iR\text{-}free}$, while the cell with the Ta–TiO_x/KB scavengers presents only a negligible decay of 3% at 0.9 $V_{iR\text{-}free}$ and 14% at 0.8 $V_{iR\text{-}free}$. These findings show that the Ta–TiO_x scavengers play a prominent role in the improvement of the PGM-free cathode durability.

Theoretical understanding of the scavenging mechanism

To elucidate the mechanisms of radical scavenging on the Ta–TiO_x nanoparticles, we employed density functional theory (DFT) calculations to investigate the interactions of ·OH, HO_2· and H_2O_2 with different oxide surfaces and identify the feasible reaction routes with enhanced scavenging capability. We compared the adsorption energies of H_2O_2 and related radicals (·OH and HO_2·) on the most stable surfaces of Fe–N–C, TiO_2, Ta_2O_5 and TaO_2 to evaluate their abilities to capture H_2O_2 and related radicals (Supplementary Figs. 15–21 and Supplementary Table 1). The computed surface Pourbaix diagram shows that under reaction conditions, the TaO_2(110) surface is covered with 1 ML OH*(Supplementary Fig. 21). As shown in Fig. 6a, the TaO_2–OH(110) surface has stronger adsorption energies than Fe–N–C for H_2O_2, ·OH and HO_2·, suggesting that it is more competitive at capturing H_2O_2 and related radicals, which can help impede their attack to the Fe–N–C active sites. The most stable adsorption structures of ·OH and HO_2· on the TaO_2–OH surface are illustrated in Fig. 6b in which the radicals are bridged between the sixfold coordinated Ta- and OH-bonded fourfold coordinated Ta sites. All the calculated electronic energies can be found in Supplementary Table 1.

To further understand the catalytic mechanisms of H_2O_2 decomposition on the TaO_2–OH surface, we computed the energy profiles for all possible pathways for H_2O_2/radicals decomposition, including direct dehydrogenation, O*-assisted pathway, OH*-assisted pathway and O* + O* recombination[37]. We find that the OH*- and O*-assisted pathways, as shown in Fig. 6c, provide the most energetically efficient route to scavenge radicals and produce H_2O and O_2. Both reaction pathways start with a homolytic O–O bond scission step in which two OH* species are the initial intermediates generated during H_2O_2 decomposition. In the O*-assisted pathway, OH* species were further disproportionated to form O* and H_2O*, whereas the OH*-assisted pathway can bypass this step to directly form OOH* and H_2O*. Both pathways contain a subsequent rapid H-transfer step for the completion of the disproportionation reaction routes. It is worth noting that the first step of H_2O_2 decomposition on the TaO_2–OH surface shows a relatively moderate energy, thus making it a promising candidate for Pt-like H_2O_2 and radical scavenging[38,39].

Conclusion

In summary, our results demonstrate the effectiveness of the Ta–TiO_x nanoparticles in scavenging ·OH and HO_2· radicals or chemically decomposing H_2O_2 to improve the durability of PGM-free catalysts in the ORR process. The Ta–TiO_x nanoparticles (~5 nm in size) were distributed on a KB substrate via a high-temperature pulse technique. Fluorescence spectroscopy and EPR tests show that the Ta–TiO_x nanoparticles present high radical scavenging efficiency. We demonstrated the Ta–TiO_x nanoparticles work synergistically with Fe–N–C catalysts to prolong the catalyst's durability by removing H_2O_2 molecules and radicals generated from incomplete oxygen reduction by the Fe–N–C catalysts. Indeed, the H_2O_2 yield after 10,000 cycles was suppressed to less than 2%, much smaller than that of the catalysts without scavengers. With the Ta–TiO_x scavengers, the PEM fuel cell presents a negligible current density decay of 3% at 0.9 $V_{iR\text{-}free}$ after an ADT, which is much smaller than the 33% decay of the cell without the scavengers. These Ta–TiO_x scavengers suggest a change from passively protecting catalysts to providing an active defence in the removal of H_2O_2 and radicals.

Methods

Materials. 2-Methylimidazole (mIm, 99%), $Zn(NO_3)_2 \cdot 6H_2O$ (>99%) and $Fe(acac)_3$ (≥99.9%) were purchased from Sigma-Aldrich. Titanium(IV) isopropoxide ($Ti(OiPr)_4$, >98%), Tantalum(V) ethoxide, ($Ta(OEt)_5$, >99%) and DMPO were purchased from Fisher Scientific. 6CFL (97% HPLC), cobalt(II) nitrate hexahydrate (99.999%) and hydrogen peroxide (30% in DI water) were purchased from Sigma-Aldrich.

Fe–N–C catalyst synthesis. The Fe–N–C catalyst was synthesized in the following steps[17].

Step 1: synthesis of Fe(acac)3@ZIF-8. 2-Methylimizadole (3.94 g) was dissolved in 100 ml methanol in flask A. $Zn(NO_3)_2 \cdot 6H_2O$ (3.57 g) and $Fe(acac)_3$ (5.0 g) were dissolved in 100 ml methanol under ultrasound for 1 h to form a clear solution in flask B. Flask B was subsequently added into flask A with vigorous stirring (25 °C) for 24 h. The obtained precipitant was separated by filtration and washed three times with methanol and finally dried overnight at 100 °C under vacuum.

Step 2: synthesis of $Fe(mIm)_4$@ZIF-8 precursor. A dispersion of 1.0 g $Fe(acac)_3$ZIF-8, 1.0 g mIm and 100 ml methanol was heated to 140 °C (4 h in a Teflon-lined autoclave). After natural cooling down, the obtained material ($Fe(mIm)_4$@ZIF-8) was separated by filtration and washed three times with methanol and finally dried overnight at 100 °C under vacuum.

Step 3: synthesis of Fe–N–C catalyst. The powder of $Fe(acac)_3$@ZIF-8 precursor was transferred to a high-alumina rectangular tray and placed in the middle of a tube furnace. The furnace was heated to 1,000 °C with a ramping rate of 5 °C min^{-1} and kept at 1,000 °C for 1 h under flowing Ar gas and naturally cooled to room temperature (Supplementary Fig. 22).

Ta–TiO_x scavenger synthesis. The high-temperature treatment was realized by a heater made from carbon paper (size: 30 mm × 5 mm × 2 mm). The carbon paper was glued on a copper electrode with silver paste.

For the synthesis of the Ta–TiO_x nanoparticles, $Ti(OiPr)_4$ and $Ta(OEt)_5$ were employed as precursors (at Ta to Ti ratios of 2:8, 4:6, 6:4 and 8:2) that were mixed with a carbon substrate (KB, carbon nanofibers or metal–organic framework carbon) in 20 ml vials (the final weight ratio between oxides and carbon was 6:4). We then added 10 ml of absolute ethanol and 1 ml of deionized water in the vials, and the process was carried out in an Ar environment. The sample was sonicated to form a slurry. The slurry was then freeze dried for over 24 h at −47 °C and 1.8 Pa. The mixture was crushed into powder and transferred to the high-temperature heater in a glovebox under Ar atmosphere. To ensure the heating homogeneity, the powders were uniformly spread across the heater surface to a thickness of 1 mm. A Keithley 2400 Source Meter was used as a time controller[32]. A Volteq HY 6020EX power supply was employed to control the output current and voltage. The current was tuned from 0 A to 20 A and the voltage was tuned from 0 V to 60 V. The mixture was subjected to a fast high-temperature treatment (~1,500 K) by Joule heating the sample in an Ar environment for 100 ms.

Temperature control and measurement. The heating temperature was measured and adjusted by colour ratio pyrometry[32]. The heating spectrum was captured by a Vison Research Phantom Miro M110 high-speed camera. The grey-body adjusted Planck's law was employed to calculate the temperature based on the spectrum in the camera's sensitive ranges. The measurement was calibrated by a black-body infrared light source (Newport Oriel 67,000 series). The parameters were noted and maintained to guarantee stable temperature control.

Characterization. A Tescan XEIA field emission SEM was used to characterize the low-magnification morphologies of the Ta–TiO_x scavengers. The TEM images, HAADF-STEM images and energy-dispersive spectra of the scavengers were captured with a JEOL 2100 F TEM at a 200 kV acceleration voltage and a JEOL TEM-STEM ARM 200 CF equipped with HAADF detector as well as an Oxford Xmax 100TLE windowless X-ray detector. The nanoparticle sizes were measured with ImageJ software, and the total number of particles in this statistic is 128. A D8 Bruker X-ray diffraction system was used to capture the XRD data with a scan rate of 3–5° min^{-1}. The N_2 adsorption-desorption experiment was carried out with a Micromeritics ASAP 2020 Porosimeter Test Station at 77 K. The samples were degassed under vacuum at 120 °C for 6 h to remove the air and free water. Specific surface area and pore size was determined by the Brunauer–Emmett–Teller and Barrett–Joyner–Halenda methods, respectively. The X-ray photoelectron spectroscopy was carried out with a Kratos Axis 165 X-ray photoelectron spectrometer.

Fluorescence spectroscopy for radical scavenging evaluation. The radical scavenging efficacy of the as-prepared ORR catalysts (Fe–N–C and Ta–TiO_x) was evaluated using a custom-built fluorescence spectrometer. 6CFL dye, which is sensitive to radicals, was used as a fluorescence probe. In a typical experiment, a solution containing 1 ml of 50 μM 6CFL in DI water, 1 mM $Co(NO_3)_2$ and 0.5 mg of Fe–N–C or Ta–TiO_x/KB was prepared. The 6CFL fluorescent dye was excited using

a 488 nm pigtailed laser purchased from Thorlabs (P488-SF20, 488 nm, 20 mW) through a 300–700 nm bifurcated optical probe (Ocean Insight) dipped into the solution. The emitted light was collected through the bifurcated optical probe and filtered using a long pass filter with a cut-on wavelength of 500 nm (FELH0500, Thorlabs). The radicals were then generated as aliquots of H_2O_2 were added to the solution. The change in fluorescence of 6CFL at 544 nm relative to the initial intensity was measured using the bifurcated optical probe under constant stirring. After each addition of H_2O_2, the solution was continuously stirred for 5 min to allow enough time for the oxidative degradation of the dye to complete before the stable fluorescence signal was collected.

EPR spin trapping. The instrument used for EPR measurements was an X-band Bruker EMX EPR spectrometer. Field-swept spectra were taken in the magnetic field from 3,250 G to 3,750 G and are representative of four scan averages collected to achieve high signal resolution. The following instrument parameters were used: microwave power = 5.0 mW; modulation frequency = 100 kHz; modulation amplitude = 1.00 G; conversion time = 40.96 ms; and time constant = 20.48 ms. Samples were transferred to glass capillary tubes with a 1 mm outer diameter and then placed in the EPR cavity. All measurements were done at room temperature. 2,2-Diphenyl-1-picrylhydrazyl hydrate (DPPH) was used as a solid-state standard field/frequency calibration of the EPR spectra ($g_{DPPH} = 2.0036 \pm 0.0003$)[40,41]. The instrument was calibrated before each measurement by running the DPPH standard at the conditions shown above.

The data were processed by the instrument software to determine the radical concentration. The following equation was used to calculate the radical concentration, in terms of the number of spins per gram of the sample:

$$[x] = \frac{[\mathrm{std}]\, A_x R_x\, (\mathrm{scan}_x)^2\, G_{\mathrm{std}} M_{\mathrm{std}}\, (g_{\mathrm{std}})^2\, [s\,(s+1)]_{\mathrm{std}}}{A_{\mathrm{std}} R_{\mathrm{std}}\, (\mathrm{scan}_{\mathrm{std}})^2\, G_x M_x\, (g_x)^2\, [s\,(s+1)]_x} \quad (1)$$

where std represents the manganese sulfate monohydrate ($MnSO_4{\cdot}H_2O$) standard sample, x represents the experimental samples, [] is the radical concentration (spins per g), A is the area under the absorption curve, R is the degeneracy of the spectrum, G is the gain of the signal amplifier (Hz), M is the modulation amplitude (G), scan is the sweep width of the measurement (G), g is the g-value of the radical measured and s is the electron spin quantum number. More information can be found in the Supplementary Information.

Detection of hydroxyl radicals by spin trapping. Hydroxyl (·OH) radicals were produced via Fenton reaction, and DMPO was employed as a spin trapping agent to identify the ·OH radical. Experiments were conducted with H_2O_2 [9 M], $FeSO_4$ (iron source), DMPO [100 mM] and H_2SO_4. Fenton reactions were performed by mixing the reagents in the following order: DI water, H_2O_2, DMPO and $FeSO_4$ and adjusting the pH to ~3 with sulfuric acid. The experiments were conducted first without and then with the Ta–TiO_x scavengers. Immediately after mixing the reagents mentioned and starting the reaction, a capillary tube was used to measure the sample in the EPR. The measurements were repeated after 30 min, 1 h, 2 h and 3 h. The same procedure was followed with the addition of the scavengers. In this case, the scavengers were added before the DMPO.

Electrochemical measurements. All tests were performed in a three-electrode setup at an electrochemical workstation (CHI 660D) using a graphite rod as the counter electrode and a RHE reference electrode. To prepare the working electrode, 10 mg of catalyst (or 90 wt% catalyst + 10 wt% $TaTiO_x$/KB) was mixed with a 1,990 µl mixture of isopropyl alcohol (70%)/water (30%) and 10 µl of 5 wt% Nafion™ solution (Sigma-Aldrich) by sonication for 30 min to form an ink. Then, 30 µl of the ink was drop dried onto a RRDE (Pine Instruments) to cover an area of 0.2472 cm^2 (that is, a catalyst loading of ~0.6 mg cm^{-2}). The catalytic activity for ORR was tested by steady-state measurement using staircase potential control with a step of 0.025 V at intervals of 25 s from 0.0 V to 1.0 V versus RHE in O_2-saturated 0.5 M H_2SO_4 solution at room temperature and a rotation rate of 900 r.p.m. The selectivity (four electron path) of the catalyst during the ORR was determined by measuring the ring current for calculating H_2O_2 yield. Cyclic voltammetry cycles between potential of 0.6 V and 1.0 V versus RHE in O_2-saturated 0.5 M H_2SO_4 solution were performed to evaluate the ORR catalytic stability.

PEM fuel cell testing. The preparation of membrane electrode assembly (MEA) catalyst ink: 30 mg of the Fe–N–C catalyst containing 8 wt% of the Ta–TiO_x/KB radical scavengers was wetted with 360 µl of water (360 mg) and 458 µl of isopropanol (360 mg). 330 mg of 5 wt% Nafion™ binder solution was subsequently added to the wetted catalyst suspension and sonicated for 30 min. The MEA was made by brush painting the catalyst ink onto a Gore Membrane (Gore M820.15) with an area of 5.0 cm^2. The cathode catalyst loading was maintained at 6.0 mg cm^{-2}. The anode catalyst loading was 0.2 mg_{Pt} cm^{-2} of Pt/C (Tananka K.K., 46.5% Pt), which was coated on a carbon paper that acted as a gas-diffusion layer. Another gas-diffusion layer (SIGRACET-GDL 29 BC) was placed on the cathode side of the membrane while assembling the MEA. Fuel cell polarization curves were recorded at 100% relative humidity and 80 °C under 1.0 bar H_2/O_2. The PEM fuel cell durability tests were carried out using a voltage-step protocol comprised of 20 cycles of holding potential at 0.85 V for 5 min and 0.40 V for 55 min (duration = 20 h) under 1.0 bar H_2/air at a cell temperature of 80 °C.

Computational method. The Vienna ab initio simulation package[42,43] was used to carry out spin polarized DFT calculations. The Perdew, Burke and Ernzerhof[44] functional was applied for the electron exchange correlation. For the ion–electron interaction, the projector augmented wave method[45] was used. A plane-wave cutoff of 400 eV, a self-consistent field convergence criterion of 1×10^{-4} eV and a maximum force of 0.025 eV $Å^{-1}$ were employed in the calculations. A 3 × 3 × 1 Monkhorst–Pack k-point mesh was used for the 2 × 2 super cells of TaO_2(110), Ta_2O_5(100) and TiO_2(101) which contain three metal oxide layers each. A 15 Å vacuum was added along the z direction to avoid artificial interactions. The adsorbates and the topmost layers of the slabs were relaxed, and the bottom two layers of the slabs were fixed for the structure optimizations. The adsorption energies of the radicals and H_2O_2 on the surface were calculated by using H_2O as a reference in combination with the computational hydrogen electrode[46]. Specifically, the adsorption energies of ·OH and HO_2· and H_2O_2 are obtained from $\Delta E_{\cdot OH} = E_{*OH} - E_{slab} - \left(E_{H_2O} - \frac{1}{2}E_{H_2}\right)$, $\Delta E_{HO_2\cdot} = E_{*OOH} - E_{slab} - \left(2E_{H_2O} - \frac{3}{2}E_{H_2}\right)$ and $\Delta E_{H_2O_2} = E_{*H_2O_2} - E_{slab} - (2E_{H_2O} - E_{H_2})$, respectively. E_{*OH}, E_{*OOH} and $E_{*H_2O_2}$ are the total energies of the slab with adsorbed ·OH and HO_2· and H_2O_2, respectively. E_{slab} is the total energy of the slab without adsorbate. E_{H_2O} and E_{H_2} are the total energies of free H_2O and H_2 molecules in the gas phase, respectively. A negative value of ΔE suggests favourable absorption[47].

Data availability

The authors declare that all data supporting the findings of this study are available within the paper and Supplementary Information files. Source data are provided with this paper.

Received: 25 February 2021; Accepted: 3 February 2022;
Published online: 25 March 2022

References

1. Shao, M., Chang, Q., Dodelet, J. P. & Chenitz, R. Recent advances in electrocatalysts for oxygen reduction reaction. *Chem. Rev.* **116**, 3594–3657 (2016).
2. Wang, X. X., Swihart, M. T. & Wu, G. Achievements, challenges and perspectives on cathode catalysts in proton exchange membrane fuel cells for transportation. *Nat. Catal.* **2**, 578–589 (2019).
3. Li, M. et al. Ultrafine jagged platinum nanowires enable ultrahigh mass activity for the oxygen reduction reaction. *Science* **354**, 1414–1419 (2016).
4. Jasinski, R. A new fuel cell cathode catalyst. *Nature* **201**, 1963–1964 (1964).
5. Gewirth, A. A., Varnell, J. A. & Diascro, A. M. Nonprecious metal catalysts for oxygen reduction in heterogeneous aqueous systems. *Chem. Rev.* **118**, 2313–2339 (2018).
6. Setzler, B. P., Zhuang, Z., Wittkopf, J. A. & Yan, Y. Activity targets for nanostructured platinum-group-metal-free catalysts in hydroxide exchange membrane fuel cells. *Nat. Nanotechnol.* **11**, 1020–1025 (2016).
7. Zhang, H. et al. Single atomic iron catalysts for oxygen reduction in acidic media: particle size control and thermal activation. *J. Am. Chem. Soc.* **139**, 14143–14149 (2017).
8. Primbs, M. et al. Establishing reactivity descriptors for platinum group metal (PGM)-free Fe–N–C catalysts for PEM fuel cells. *Energy Environ. Sci.* **13**, 2480–2500 (2020).
9. Luo, F. et al. *P*-block single-metal-site tin/nitrogen-doped carbon fuel cell cathode catalyst for oxygen reduction reaction. *Nat. Mater.* **19**, 1215–1223 (2020).
10. Lefèvre, M., Proietti, E., Jaouen, F. & Dodelet, J. P. Iron-based catalysts with improved oxygen reduction activity in polymer electrolyte fuel cells. *Science* **324**, 71–74 (2009).
11. Proietti, E. et al. Iron-based cathode catalyst with enhanced power density in polymer electrolyte membrane fuel cells. *Nat. Commun.* **2**, 416 (2011).
12. Zhang, G., Chenitz, R., Lefèvre, M., Sun, S. & Dodelet, J. P. Is iron involved in the lack of stability of Fe/N/C electrocatalysts used to reduce oxygen at the cathode of PEM fuel cells? *Nano Energy* **29**, 111–125 (2016).
13. Shao, Y., Dodelet, J. P., Wu, G. & Zelenay, P. PGM-free cathode catalysts for PEM fuel cells: a mini-review on stability challenges. *Adv. Mater.* **31**, 1807615 (2019).
14. Choi, C. H. et al. The Achilles' heel of iron-based catalysts during oxygen reduction in an acidic medium. *Energy Environ. Sci.* **11**, 3176–3182 (2018).
15. Chenitz, R. et al. A specific demetalation of Fe–N_4 catalytic sites in the micropores of NC–Ar + NH_3 is at the origin of the initial activity loss of the highly active Fe/N/C catalyst used for the reduction of oxygen in PEM fuel cells. *Energy Environ. Sci.* **11**, 365–382 (2018).
16. Schmies, H. et al. Unravelling degradation pathways of oxide-supported Pt fuel cell nanocatalysts under in situ operating conditions. *Adv. Energy Mater.* **8**, 1701663 (2018).

17. Xie, X. et al. Performance enhancement and degradation mechanism identification of a single-atom Co–N–C catalyst for proton exchange membrane fuel cells. *Nat. Catal.* https://doi.org/10.1038/s41929-020-00546-1 (2020).
18. Jaouen, F. O_2 reduction mechanism on non-noble metal catalysts for PEM fuel cells. Part II: a porous-electrode model to predict the quantity of H_2O_2 detected by rotating ring-disk electrode. *J. Phys. Chem. C.* **113**, 15433–15443 (2009).
19. Lefèvre, M. & Dodelet, J. P. Fe-based catalysts for the reduction of oxygen in polymer electrolyte membrane fuel cell conditions: determination of the amount of peroxide released during electroreduction and its influence on the stability of the catalysts. *Electrochim. Acta* **48**, 2749–2760 (2003).
20. Kumar, K. et al. On the influence of oxygen on the degradation of Fe–N–C catalysts. *Angew. Chem.* **132**, 3261–3269 (2020).
21. Goellner, V., Armel, V., Zitolo, A., Fonda, E. & Jaouen, F. Degradation by hydrogen peroxide of metal–nitrogen–carbon catalysts for oxygen reduction. *J. Electrochem. Soc.* **162**, H403–H414 (2015).
22. Qiao, Z. et al. 3D porous graphitic nanocarbon for enhancing the performance and durability of Pt catalysts: a balance between graphitization and hierarchical porosity. *Energy Environ. Sci.* **12**, 2830–2841 (2019).
23. Gadipelli, S., Zhao, T., Shevlin, S. A. & Guo, Z. Switching effective oxygen reduction and evolution performance by controlled graphitization of a cobalt–nitrogen–carbon framework system. *Energy Environ. Sci.* **9**, 1661–1667 (2016).
24. Gouérec, P. et al. Dioxygen reduction electrocatalysis in acidic media: effect of peripheral ligand substitution on cobalt tetraphenylporphyrin. *J. Electroanal. Chem.* **398**, 67–75 (1995).
25. Gouérec, P. et al. Oxygen reduction in acid media catalysed by heat treated cobalt tetraazaannulene supported on an active charcoal: correlations between the performances after longevity tests and the active site configuration as seen by XPS and ToF-SIMS. *J. Electroanal. Chem.* **422**, 61–75 (1997).
26. Bezerra, C. W. B. et al. A review of heat-treatment effects on activity and stability of PEM fuel cell catalysts for oxygen reduction reaction. *J. Power Sources* **173**, 891–908 (2007).
27. Alves, M. C. M., Dodelet, J. P., Guay, D., Ladouceur, M. & Tourillon, G. Origin of the electrocatalytic properties for O_2 reduction of some heat-treated polyacrylonitrile and phthalocyanine cobalt compounds adsorbed on carbon black as probed by electrochemistry and X-ray absorption spectroscopy. *J. Phys. Chem.* **96**, 10898–10905 (1992).
28. Ladouceur, M. et al. Pyrolyzed cobalt phthalocyanine as electrocatalyst for oxygen reduction. *J. Electrochem. Soc.* **140**, 1974–1981 (2019).
29. Kolthoff, H. M. & Medalia, A. I. The reaction between ferrous iron and peroxides. III. Reaction with cumene hydroperoxide, in aqueous solution. *J. Am. Chem. Soc.* **71**, 3789–3792 (1949).
30. Kramm, U. I. et al. On an easy way to prepare metal–nitrogen doped carbon with exclusive presence of MeN_4-type sites active for the ORR. *J. Am. Chem. Soc.* **138**, 635–640 (2016).
31. Jaouen, F. & Dodelet, J. P. O_2 reduction mechanism on non-noble metal catalysts for PEM fuel cells. Part I: experimental rates of O_2 electroreduction, H_2O_2 electroreduction, and H_2O_2 disproportionation. *J. Phys. Chem. C.* **113**, 15422–15432 (2009).
32. Xie, H. et al. High-temperature pulse method for nanoparticle redispersion. *J. Am. Chem. Soc.* **142**, 17364–17371 (2020).
33. Syono, Y., Kikuchi, M., Goto, T. & Fukuoka, K. Formation of rutile-type Ta(IV)O_2 by shock reduction and cation-deficient $Ta_{0.8}O_2$ by subsequent oxidation. *J. Solid State Chem.* **50**, 133–137 (1983).
34. Edgecomb, J. et al. Mapping localized peroxyl radical generation on a PEM fuel cell catalyst using integrated scanning electrochemical cell microspectroscopy. *Front. Chem.* **8**, 572563 (2020).
35. Prabhakaran, V., Arges, C. G. & Ramani, V. Investigation of polymer electrolyte membrane chemical degradation and degradation mitigation using in situ fluorescence spectroscopy. *Proc. Natl Acad. Sci. USA* **109**, 1029–1034 (2012).
36. Matuszak, Z., Reszka, K. J. & Chignell, C. F. Reaction of melatonin and related indoles with hydroxyl radicals: EPR and spin trapping investigations. *Free Radic. Biol. Med.* **23**, 367–372 (1997).
37. Plauck, A., Stangland, E. E., Dumesic, J. A. & Mavrikakis, M. Active sites and mechanisms for H_2O_2 decomposition over Pd catalysts. *Proc. Natl Acad. Sci. USA* **113**, E1973–E1982 (2016).
38. Laursen, A. B., Man, I. C., Trinhammer, O. L., Rossmeisl, J. & Dahl, S. The Sabatier principle illustrated by catalytic H_2O_2 decomposition on metal surfaces. *J. Chem. Educ.* **88**, 1711–1715 (2011).
39. Balbuena, P. B., Calvo, S. R., Lamas, E. J., Salazar, P. F. & Seminario, J. M. Adsorption and dissociation of H_2O_2 on Pt and Pt-alloy clusters and surfaces. *J. Phys. Chem. B* **110**, 17452–17459 (2006).
40. Poole, C. P. *Electron Spin Resonance: A Comprehensive Treatise on Experimental Techniques* 2nd edn, (Wiley, 1983).
41. Lee, Y.-K., Whittaker, M. M. & Whittaker, J. W. The electronic structure of the Cys-Tyrúýfree radical in galactose oxidase determined by EPR spectroscopy. *Biochemistry* **47**, 6637–6649 (2008).
42. Kresse, G. & Furthmüller, J. Bayesian optimization for calibrating and selecting hybrid-density functional models. *Phys. Rev. B* **54**, 11169–11186 (1996).
43. Kresse, G. & Furthmüller, J. Efficiency of ab-initio total energy calculations for metals and semiconductors using a plane-wave basis set. *Comput. Mater. Sci.* **6**, 15–50 (1996).
44. Perdew, J. P., Burke, K. & Ernzerhof, M. Generalized gradient approximation made simple. *Phys. Rev. Lett.* **77**, 3865–3868 (1996).
45. Blöchl, P. E. Projector augmented-wave method. *Phys. Rev. B* **50**, 17953 (1994).
46. Lu, Z. et al. High-efficiency oxygen reduction to hydrogen peroxide catalysed by oxidized carbon materials. *Nat. Catal.* **1**, 156–162 (2018).
47. Nørskov, J. K. et al. Origin of the overpotential for oxygen reduction at a fuel-cell cathode. *J. Phys. Chem. B* **108**, 17886–17892 (2004).

Acknowledgements

L.H., Y.S., X.X. and H.X. acknowledge support from the US Department of Energy, Office of Energy Efficiency and Renewable Energy and Hydrogen and Fuel Cell Technologies Office through the Electrocatalysis consortium (ElectroCat) and from DOE programme managers D. Papageorgopoulos, S. Thompson, D. Peterson and G. Kleen. R.S.-Y. acknowledges financial support from National Science Foundation DMR-1809439. D.J. acknowledges support from the National Science Foundation CHE-2102191. G.H. acknowledges the financial support from the Queens College, City University of New York. The authors acknowledge the support of the Maryland Nanocenter, its Surface Analysis Center and AIMLab. The views and opinions of the authors expressed herein do not necessarily state or reflect those of the US government or any agency thereof. Neither the US government nor any agency thereof, nor any of their employees, makes any warranty, expressed or implied, or assumes any legal liability or responsibility for the accuracy, completeness or usefulness of any information, apparatus, product or process disclosed, or represents that its use would not infringe privately owned rights.

Author contributions

L.H. and Y.S. co-supervised the research. L.H., Y.S., V.P. and H.X. conceived the concept. H.X., X.X., Y.S. and L.H. designed the experiment. H.X. and X.X. carried out the experimental works including syntheses and electrochemical measurements. H.X., M.H., M.W. and A.H.P. carried out the characterization of materials. H.X., L.G.-L. and M.I.A.-S. carried out the EPR test. V.P. carried out the fluorescence test. S.S. and V.R. conducted the fuel cell test. G.H. and D.J. carried out the calculation analysis. H.X. and L.H. wrote the paper. G.H, X.X., R.S.-Y. and Y.S. revised the paper. All authors contributed to the discussion of the manuscript.

Competing interests

The authors declare no competing interests.

Additional information

Supplementary information The online version contains supplementary material available at https://doi.org/10.1038/s41560-022-00988-w.

Correspondence and requests for materials should be addressed to Guoxiang Hu, Reza Shahbazian-Yassar, Yuyan Shao or Liangbing Hu.

Peer review information *Nature Energy* thanks Frédéric Jaouen, Ulrike Kramm and Samira Siahrostami for their contribution to the peer review of this work.